

Fragility and volatility of structural hubs in the human connectome

Leonardo L. Gollo^{1,2*}, James A. Roberts^{1,2}, Vanessa L. Cropley³, Maria A. Di Biase^{3,4}, Christos Pantelis^{3,5,6}, Andrew Zalesky^{3,7} and Michael Breakspear^{1,2,8*}

Brain structure reflects the influence of evolutionary processes that pit the costs of its anatomical wiring against the computational advantages conferred by its complexity. We show that cost-neutral ‘mutations’ of the human connectome almost inevitably degrade its complexity and disconnect high-strength connections to prefrontal network hubs. Conversely, restoring the peripheral location and strong connectivity of empirically observed hubs confers a wiring cost that the brain appears to minimize. Progressive cost-neutral randomization yields daughter networks that differ substantially from one another and results in a topologically unstable phenomenon consistent with a phase transition in complex systems. The fragility of hubs to disconnection shows a significant association with the acceleration of gray matter loss in schizophrenia. Together with effects on wiring cost, we suggest that fragile prefrontal hub connections and topological volatility act as evolutionary influences on brain networks whose optimal set point may be perturbed in neuropsychiatric disorders.

The brain draws a disproportionate metabolic load from the body. Reducing the cost of metabolic consumption is expressed through many facets of brain activity and structure, from sparse spikes to the parsimonious principles underlying structural brain networks¹. Minimizing wiring length reduces the cost associated with building and maintaining long axons and addresses the ‘packing problem’ of fitting the brain into a modest three-dimensional volume. However, the minimization of metabolic load must be balanced against the need to undertake complex cognitive functions at speed. Since structure reflects function², this entails an opposing trend toward increasingly complex topological properties of the human connectome, including the presence of hierarchies³, richly interconnected hubs⁴, and structural modules⁵. Such non-trivial topological properties of the human connectome inevitably come at a wiring-length cost⁶, most strikingly expressed through the presence of long hub-to-hub connections⁷.

Different species display different solutions to this trade-off, from small brains with fixed behavioral repertoires through to the metabolically hungry but cognitively sophisticated human brain. Considerable research has addressed this issue, uncovering broad principles such as the allometric scaling of white matter volume and gray matter surface area across species^{8,9}. In recent years, whole-brain tractography reconstructed from diffusion MRI has allowed increasingly nuanced characterization of human brain topology¹. However, even if the wiring length and topological properties of the human brain were accurately known, efforts to understand the complexity–parsimony trade-off would still face a considerable challenge: what would the wiring cost and/or topological complexity be if the relative importance of each were weighted differently? While comparisons to other species are informative^{1,9}, the gap between the human brain and nonhuman primate brain is

considerable¹⁰. The nature of the complexity–parsimony trade-off thus remains unknown.

The adaptability and parsimony of a species is critical to inter-generational survival. However, from an evolutionary standpoint, population variability and diversity are also needed to minimize extinction risk due to environmental changes to which a homogeneous species cannot successfully adapt¹¹: a species with insufficient diversity risks occupying a narrow ecological niche that lacks resilience to environmental dynamics¹². While judicious genetic mutation is one solution to this problem, the background genetic variability in a species can be thought of as a natural reserve, that is, the ability of a species to adapt to environmental changes. However, species also require a probabilistic identity—that is, an upper limit on the variance of this diversity—to support a common syntax for exchange, reciprocity, and reproduction¹³. Understanding the principles underlying structural diversity may also shed light on variations in network structure that lie outside of the normal spectrum, such as those that accompany schizophrenia¹⁴ and other brain disorders.

Since the seminal ‘small-world’ paper by Watts and Strogatz, network randomization techniques have played an important role in studying system topology¹⁵. Random networks that retain basic features of an empirical network, such as the number of nodes and connections, serve as important benchmarks in the study of empirical networks¹⁶. Extensions of this approach, using rewiring algorithms, have highlighted the highly nontrivial properties of the human connectome, such as its small-world topology¹⁷. However, many interesting networks such as the brain are spatially embedded, comprised of nodes with a physical location and edges whose physical substrate carries a cost. Crucially, most rewiring algorithms do not preserve wiring length, yielding benchmark networks with

¹QIMR Berghofer Medical Research Institute, Brisbane, Queensland, Australia. ²Centre of Excellence for Integrative Brain Function, QIMR Berghofer Medical Research Institute, Brisbane, Queensland, Australia. ³Melbourne Neuropsychiatry Centre, Department of Psychiatry, The University of Melbourne and Melbourne Health, Melbourne, Victoria, Australia. ⁴Psychiatry Neuroimaging Laboratory, Department of Psychiatry, Brigham and Women’s Hospital, Harvard Medical School, MA, USA. ⁵Centre for Neural Engineering, Department of Electrical and Electronic Engineering, The University of Melbourne, Melbourne, Victoria, Australia. ⁶Florey Institute of Neuroscience and Mental Health, The University of Melbourne, Parkville, Victoria, Australia.

⁷Department of Biomedical Engineering, The University of Melbourne, Melbourne, Victoria, Australia. ⁸Metro North Mental Health Service, Brisbane, Queensland, Australia. *e-mail: leonardo.gollo@qimrberghofer.edu.au; michael.breakspear@qimrberghofer.edu.au

substantially longer wiring lengths than the actual brain, thus being more metabolically costly and less parsimonious¹⁸. Nongeometric benchmark networks play a crucial role in identifying nonrandom features of complex networks, but unless they are carefully curated to retain spatial embedding^{6,19–21}, their use in understanding the parsimony–complexity trade-off in the human brain is limited.

We addressed this problem by applying a rewiring algorithm that preserves the complex dependence between connectivity strength and distance in connectomic data. In particular, by characterizing the local neighborhood of empirical structural connectomes (by incremental randomization) as well as the global space (by full randomization), we examined the trade-offs between wiring, topology, complexity, and diversity expressed in empirical connectomes. We studied the fragility of high-degree hubs to disconnection through cost-preserving perturbations, as well as the topological variability between different realizations of incremental randomizations of the human connectome. This latter issue speaks to connectome diversity at the species level and provides insights into the landscape in which human connectomes are embedded. We finally hypothesized that fragile network hubs may be more vulnerable to neurodevelopmental or pathological insults and may hence predict the gray matter loss that occurs in schizophrenia²². We examined the correlations of hub fragility to brain morphology in a cohort of schizophrenia patients and controls, as well as the age of illness onset in the clinical cohort.

Results

We studied a weighted structural connectome reconstructed from diffusion MRI data in 75 healthy adults. From this empirical connectome, we explored the landscape of incrementally perturbed random surrogate connectomes obtained by randomizing the weights of the connections using one of two methods (Fig. 1a and Supplementary Fig. 1): (i) a classic geometry-ignoring randomization (R_w), obtained by randomly shuffling the location of the weights in the connectivity matrix, and (ii) a recently developed geometry-preserving randomization (G_w), obtained by taking into account the strong influence of interareal distance on the weight of anatomical connections⁶.

Geometric brain surrogates, hubs, and their spatial distribution.

It has been previously shown that random graphs that preserve the distance–weight relationship of neural systems retain many, but not all, of their topological features^{6,19–21}. One property that is incompletely retained is the nature of hubs (nodes with high-strength connections, where the node strength is the sum of the weights of the connections). In particular, while G_w surrogates do possess hubs, their distribution of strengths is narrower (they have fewer and less-prominent strong hubs) and their spatial distribution is markedly different, with hubs clustered in the center of the brain (Fig. 1a). By preserving the presence and spatial position of the hubs in the brain, it is possible to generate more highly constrained geometric surrogates. We explored two possibilities: (i) restoring the strength distribution, yielding networks G_s whose hubs have the same connectivity as those in the original connectome, but are now positioned as randomly determined, and (ii) restoring the entire strength–sequence distribution, yielding networks G_{ss} with the original set of hubs in their original positions⁶. That is, these more-refined surrogate networks (Fig. 1a) have hubs in geometrically constrained random positions (G_s) or have hubs in the same positions as in the original brain (G_{ss}). These two adjustments allow us to disambiguate the cost of having high-degree hubs per se from any putative additional costs and benefits of having those high-degree hubs in their empirically observed locations. The edges in these highly constrained surrogates also preserve the distance–weight relationship (i.e., the spatial embedding) but are otherwise randomly arranged. Topological properties unique to the original connectome (absent in the surrogates) reflect additional, specific wiring rules⁶.

We also applied strength adjustments to the geometry-ignoring surrogate networks (R_w) to recover randomly located high-strength hubs (R_s) and originally located hubs (R_{ss}). In contrast with prior research, we introduced randomization progressively, from 0 to 100% of the connections (Fig. 1b). This enabled exploration of incremental perturbations and thus the analysis of the local stochastic neighborhood of the connectome.

Wiring cost. We first used these six distinct surrogate methods (three geometry-preserving G (G_w , G_s , G_{ss}) and three geometry-ignoring R (R_w , R_s , R_{ss}) methods) to study the cost of the brain's white matter. This was estimated using the fiber (streamline) length (Supplementary Fig. 2) and the wiring cost (Fig. 2), namely, the product of the fiber length and the connection weight. The wiring cost for the simplest geometric surrogate (G_w) is, by construction, constant across all fractions of randomized edges (Fig. 2a). In contrast, reintroducing high-strength hubs via the strength adjustment algorithm impacts (weakly) upon wiring cost: in the presence of hubs (G_s), a small fraction of randomized links increases the wiring cost of the empirical connectome (Fig. 2b). The results are almost identical when using fiber lengths instead of wiring cost (Supplementary Fig. 2). Note that this is a probabilistic result across a large ensemble of random networks, but is highly robust: a reduction in the wiring cost is very unlikely to occur by small perturbations of the network (Supplementary Fig. 3). At 0.02% randomization (the peak in Supplementary Fig. 3b), some 25% of surrogates have a shorter wiring cost. This is because the variance of wiring cost amongst the surrogates initially increases faster than the corresponding increase in the mean wiring cost. When considering all surrogates with <0.05% randomization (the full range of Supplementary Fig. 3b), only 2.0% of all surrogates have a shorter wiring length. The chance of reducing the wiring cost falls below 0.1% for a fraction of randomized links greater than 0.15% (corresponding to ~100–200 randomized edges). However, for fractions of randomized links above 35% the trend is inverted and the wiring cost becomes smaller than the original brain (Fig. 2b). However, with this depth of randomization, hubs have dramatically shifted in position.

Resetting the hub's locations to match the original brain (G_{ss}) produces a more substantial increase in the wiring cost that grows monotonically with randomization (Fig. 2c). Such perturbed networks have, for an extremely limited fraction of randomized edges (<0.001), a low probability of being less costly than the original brain (Supplementary Fig. 3). The fully randomized (strength–sequence-preserving) brain possesses an increased wiring cost of $6.0 \pm 0.2\%$ (mean \pm s.d.). The estimated extra cost increases further for more sparsely thresholded connectomes (Supplementary Fig. 4).

In contrast to these geometry-preserving surrogates, which predict a modest extra wiring cost, geometry-ignoring surrogates R lead to an increase in wiring cost of 112–122% (Fig. 2d). A doubling of the white matter length is unlikely to be physically realizable, given volumetric constraints of the brain.

Structural hemisphericity. The simplest possible decomposition of the brain is into its two hemispheres. Most axon bundles cross hemispheres via the corpus callosum, a major white matter tract that has a limited volume. The density of long-range inter-hemispheric connections constitutes 13% of all corticocortical connections (Fig. 3a). These connections are also longer than their Euclidean distance, because the fibers converge, are bundled, and follow specific white matter pathways that are often much longer than the minimal (straight-line) distance. Without imposing geometric constraints, surrogate networks (R) linearly increase the density of inter-hemispheric connections (more than threefold, from 13% to 50%) until a single homogeneous brain is reached (Fig. 3a).

Imposing a geometric constraint (labeled G in Fig. 3a) limits the number of long-range connections and therefore the number of

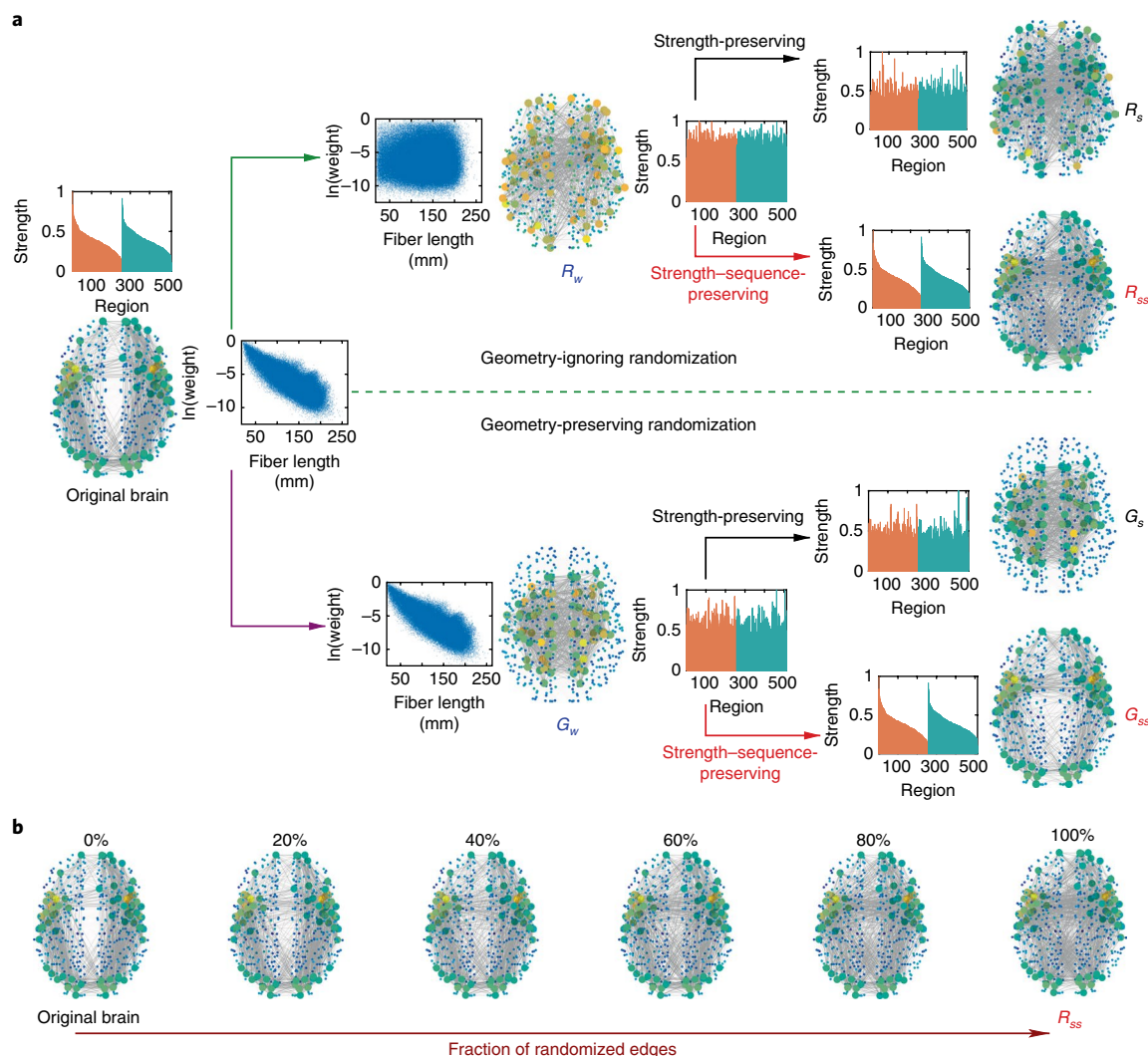


Fig. 1 | Schematic of surrogate network methods. a, Beginning with the original brain (left), we generate a hierarchy of surrogates. We visualize each network from above, showing the top 75 nodes by strength (hubs; large circles; warmer colors represent higher strengths), nonhubs (small dots), and hub-to-hub connections (gray lines). For all networks, we also show the sets of strengths, ordered by their decreasing order in the original brain for the left (orange) and right (teal) hemispheres. There are two steps in the hierarchy: (i) randomization of the connectivity matrix, either geometry-ignoring (top half) or geometry-preserving (bottom half), the distinction being whether the weight-distance relationship (blue clouds of points) is preserved (following purple arrow), giving the weight-preserving geometric surrogate G_w , or scrambled (following green arrow), giving the weight-preserving random surrogate R_w ; and (ii) retrieval of the original strengths in one of two ways: hub (or strength)-preserving (following black arrows), by adjusting the weights to give the original set of node strengths but in an order arising by chance, giving surrogates G_s and R_s , which have hubs with the same strength as the empirical brain but not necessarily located at the same positions; or hub-position- (or strength-sequence)-preserving (following red arrows), that is, preserving the original node strengths in their original order, giving surrogates G_{ss} and R_{ss} , which have hubs with the same strength and position as the empirical brain. Their connectivity is illustrated in Supplementary Fig. 1. **b**, An example of a partial randomization scheme in which only a desired fraction of edges is chosen for randomization (illustrated here on the R_{ss} surrogate), giving a tunable degree of randomization that interpolates between the original brain and the surrogate networks. Panels correspond to a single illustrative trial.

inter-hemispheric connections. Although growth in the proportion of inter-hemispheric connections occurs, it is limited to an increase of 8%, about 1/5 of the increase that accompanies nongeometric randomization.

Connections between homologous regions across hemispheres are thought to play a crucial role in the integration of neuronal activity²³. Direct homologous connections occur in 50% of regions of the original brain (compared to the overall connectivity, which is set by the threshold to 30%). However, despite the increase in the proportion of inter-hemispheric connections with progressive edge randomization, the number of homologous connections decays in all benchmark networks (Fig. 3b). Again, the geometry-preserving factor in the randomization process (G) bounds the proportion of

homologous connections to 37–40%, whereas geometry-ignoring randomizations (R) lead to 30% homologous connections. This equates to the chance level for a network with a density of 30% (see Supplementary Fig. 5 for other densities).

Network topology and complexity. Spatially embedded networks that possess long-range edges are canonical examples of small-world networks¹⁷. Randomizing edges reduces the clustering coefficient C , the mean path length L , and the small-world index (Fig. 3c and Supplementary Fig. 5). Although this reduction occurs for both geometry-preserving (G) and geometry-ignoring (R) surrogates, the preservation of distance-dependence for G surrogates means that spatially proximate nodes remain connected amongst

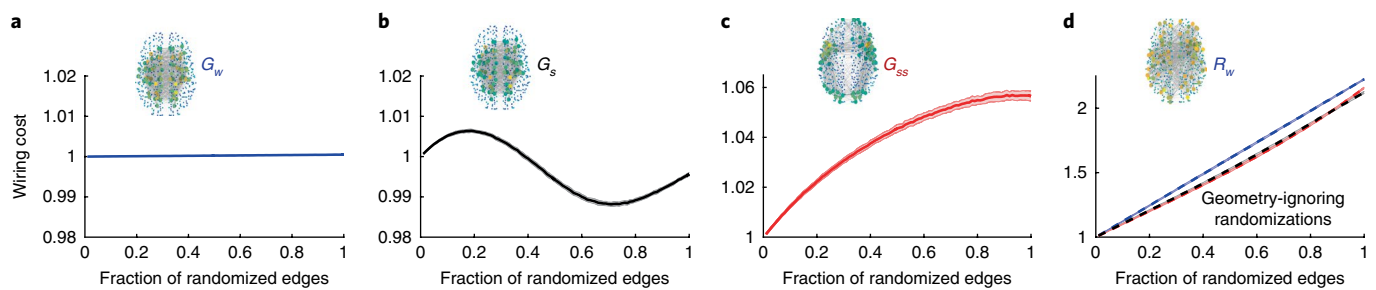


Fig. 2 | Wiring costs as a function of the fraction of randomized edges. **a**, Weight-preserving geometric surrogate, G_w (blue). **b**, Strength-preserving geometric surrogate, G_s (black). **c**, Strength-sequence-preserving geometric surrogate, G_{ss} (red). **d**, Geometry-ignoring random surrogates R_w (blue), R_s (black), and R_{ss} (red). All y axes are normalized to the original brain; note the different scales. Connectomes at the top of each panel illustrate one case in which all edges have been randomized. Shaded areas indicate the s.d. of the mean over $n=100$ trials. Blue curves, R_w (dashed) and G_w (continuous); black curves, R_s (dashed) and G_s (continuous); red curves, R_{ss} (dashed) and G_{ss} (continuous).

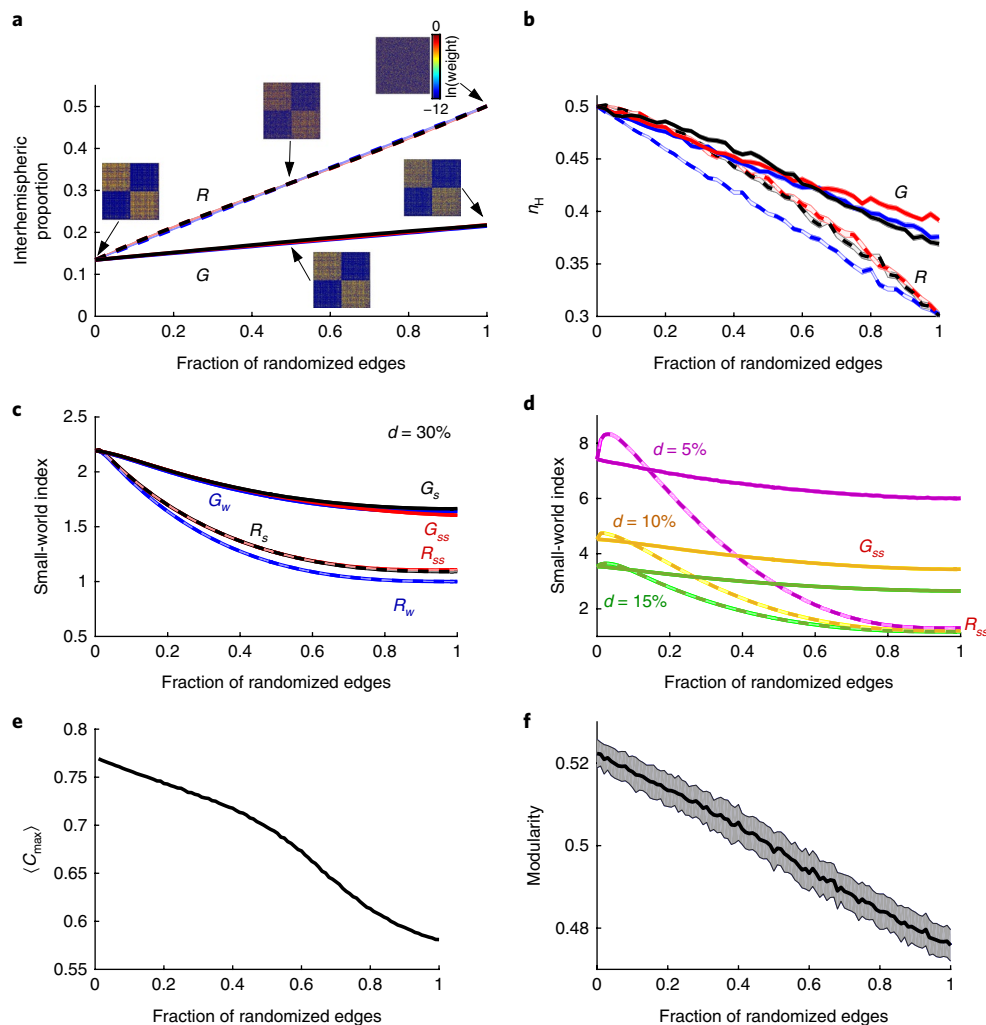


Fig. 3 | Fundamental structural features of the connectome. **a**, Proportion of connections between hemispheres for connectomes with a density of 30%. R , geometry-ignoring surrogates; G , geometry-preserving surrogates. Insets: exemplar weighted-connectivity matrices. Blue curves, R_w (dashed) and G_w (continuous); black curves, R_s (dashed) and G_s (continuous); red curves, R_{ss} (dashed) and G_{ss} (continuous). **b**, Proportion of homologous connections (n_H) between (symmetric regions of the two hemispheres). **c**, Evolution of small-worldness for the different connectomes. **d**, Evolution of small-worldness for the different network densities ($d=5\%$, 10% , 15%) with G_{ss} as continuous lines and R_{ss} as dashed lines. **e**, Mean functional complexity for G_s . **f**, Mean modularity for G_s using the Louvain community algorithm with $\gamma=1$. Shaded area indicates the s.d. of the mean over $n=100$ trials.

each other, forming local cliques and preserving clustering. This effect halves the final reduction in the small-world index compared to geometry-ignoring surrogates (R).

For a small fraction of geometry-ignoring randomized edges, however, the small-world index increases (particularly in sparser networks; Fig. 3d). Because the small-world index depends on C/L ,

the initial addition of a few costly long-range edges causes a faster decrease in L than in C , leading to an increase in the small-worldness (Supplementary Fig. 5). This finding suggests that the brain is only wired to maximize small-worldness when taking its spatial embedding into account.

Complex structural networks are adaptive to the extent that they support complex dynamics. We next used a measure of functional complexity that estimates the balance between completely random versus completely synchronized activity that would arise from dynamics unfolding on these networks²⁴ (see Methods). This measure of functional complexity decreases monotonically with increasing depth of geometrically constrained randomization (Fig. 3e). Substantial recent work has also highlighted the functional importance of a community structure in complex networks⁵. The degree to which a network conforms to an idealized modular (community) structure can be quantified by a single modularity index, Q ⁵. We find a robust, monotonic decrease in Q (Fig. 3f) regardless of whether the networks are thresholded or not and regardless of whether the decomposition is weighted toward numerous small communities or toward a few large ones. We also measured the correlation between nodes' hub strength and their participation index, the ratio of between-module to within-module connections. We find that this correlation is negative in the empirical connectome ($r = -0.086$, s.d. = 0.015, $P < 10^{-15}$), that is, high-strength hubs tend to connect within their own modules: intermodule connections are carried by low- and medium-strength nodes. For the fully randomized networks, the correlation is positive ($r = 0.083$, s.d. = 0.013, $P < 10^{-15}$), that is, hubs tend to connect to other modules.

Considered in isolation, there are a small fraction of geometry-preserving perturbations that, by chance (against the prevailing trend), reduce the wiring cost of the connectome (Supplementary Fig. 3b). Likewise, due to their stochastic nature, such perturbations may also increase the complexity or the modularity. But when triangulated among all these metrics—lower wiring cost plus higher small-world index, complexity, and modularity—only one surrogate in 2,000 realizations meet these criteria following 0.05% randomization or less (and the fraction diminishes further with deeper randomization). Hence, while there is some room for stochastic improvements in the brain (benchmarked against these metrics), that chance is very low.

Hub locations. Hubs are thought to be of particular relevance to complex, multimodal cognitive functions²⁵. They show high metabolic consumption²⁶ and lengthy connections⁷, and they appear to be disproportionately involved in brain disorders^{27,28}. We next focused on the evolution of the position of hubs as the brain is progressively randomized whilst preserving the strength distribution (G_s), which guarantees the presence of hubs but does not anchor their location. As the fraction of random edges increases, hub positions pass through a highly variable regime, whereby their physical location differs greatly between surrogate realizations. This trend illustrates a transition between two configurations: the original brain (Fig. 4a) and a final configuration that is fairly consistent across trials (Fig. 4b). For relatively modest randomization, connections to prefrontal hubs are the first to be disrupted, losing strength almost immediately and losing their hub status completely after 30–40% of edges are randomized. Between 50% and 60% randomization, we find large variability across trials, such that most of the remaining hubs undergo a substantial restructuring, with posterior hubs tending to lose their hub status. As the process advances, the location of hubs shifts toward the geometric center of the brain, forming a dense cluster (see Supplementary Videos 1 and 2). This intertrial variability can be measured formally by the susceptibility index, which increases monotonically until it peaks at ~65% randomization (Fig. 4c). A similar effect also occurs for functional complexity (Fig. 4d). The original brain is thus separated from fully randomized networks by a volatile intermediate region.

The strongest hubs thus progressively evolve under incremental randomization from a diffuse, peripheral arrangement to a compact, central core (Fig. 4e). Progressive changes in the strength of nodes with increasing depth of randomization reveal how connectivity shifts from frontal and posterior areas to midline nodes (20–40%). Accordingly, spatially peripheral regions lose strength, whereas central nodes gain enhanced connectivity (Fig. 4f). Only hubs deep in the original brain, in proximity to the insula, retain their hubness throughout progressive, geometry-preserving randomization.

This transition between two configurations observed in the variation in strength is corroborated by other network features. The original brain has the largest mean fiber length between hubs (Fig. 4g). This reflects the progressive shift of hubs from peripheral to central locations under network randomization and is consistent with prior reports of the high cost of the brain's highly connected rich club⁷. The s.d. of fiber length across realizations exhibits two marked peaks (Fig. 4h). One peak occurs early (~5% of edges randomized), reflecting volatile connections involving prefrontal hubs. The proximity of this first peak indicates that the brain is in a weakly stable configuration, that is, the topology of the empirical connectome is highly susceptible to slight random variations^{29,30}. The second and larger peak is associated with a general transition that is observed in multiple measures (Fig. 4c,d,h,j) although the exact peak position varies across these measures. For example, the peak in the variability (s.d.) occurs at approximately 70% randomization for functional complexity (Figs. 4d) and 50% for hub-to-hub fiber length (Fig. 4h). Note that the transition through a highly volatile intermediate regime is not a trivial outcome of randomizing networks. It does not occur with geometrically unconstrained randomization (Supplementary Fig. 6). The volatility seen in Fig. 4 reflects the unique mix of the residual order from the empirical connectome with a degree of (constrained) disorder. This yields, on individual realizations, statistically unlikely states that differ substantially from one to the other. The fully randomized G networks, although highly disordered, are all statistically likely and do not show such interindividual variability.

Analysis of the subnetwork of interhub connections shows that as the number of inter-hemispheric connections grows (Fig. 3a), the number of modules at the largest scale consistently changes from two modules to one (Fig. 4i). The density of edges in this hub-to-hub subnetwork decreases from that of the original brain to a minimum and increases again as this subnetwork approaches the compact, central configuration (Fig. 4j). This indicates two configurations of strong hub-to-hub connectivity separated by a variable and transitory regime with sparser interhub connectivity.

Hub fragility. We next quantified the probability that each hub retains its high-strength hubness as the connectome is progressively randomized using strength-preserving surrogates (G_s). The probability of being a hub, P^h , decays heterogeneously as a function of the fraction of randomization (Fig. 5a,b); some hubs are substantially more fragile than others. The first hubs to lose their hub status are located in the prefrontal cortex (Fig. 5b), followed by posterior hubs, consistent with the pattern observed in Fig. 4. A large proportion of these fragile hubs, including the prefrontal hubs, belong to the default mode and salience networks (see Supplementary Table 1). In contrast, a large proportion of hubs in the cingulo-opercular network, including the insula, are among the most resilient. Only four of the 75 original hubs are among the top 75 hubs after full randomization. Nine of the hubs are more resilient than expected by chance after complete randomization (Fig. 5c). The resilience of hubs is correlated with the original strength of the hubs ($r = 0.59$, $P < 10^{-7}$; Fig. 5d) and with the strength of hubs in the fully randomized brain ($r = 0.76$, $P < 10^{-14}$; Fig. 5e). Hence, hub resilience is the outcome of several factors, including strength, weight distribution, and spatial position. Subtle effects in each of these domains

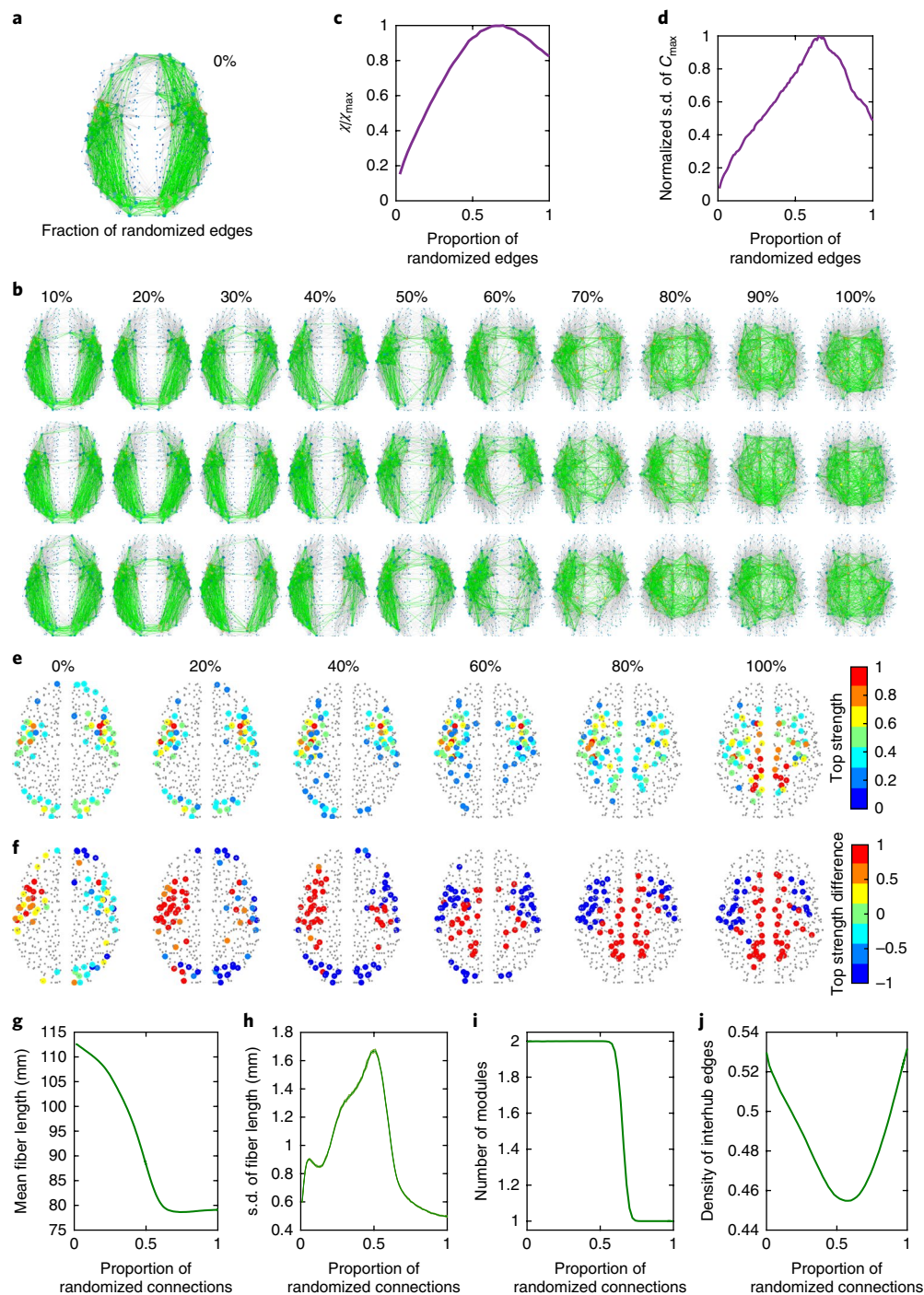


Fig. 4 | Hub variability and evolution of interhub connectivity. **a**, Original brain, representing only the top 10% strongest connections. Green edges are those between the top 75 hubs by strength. **b**, Exemplar evolution of hubs and interhub connections for three different trials. **c**, Normalized network susceptibility χ/χ_{\max} (see Methods for details). **d**, Normalized s.d. of the functional complexity (C_{\max}). **e**, Normalized strength of the top 75 nodes after averaging across networks. **f**, Normalized variation in strength of the top 75 nodes. **g**, Mean fiber length between hubs. **h**, Standard deviation (s.d.) of the mean fiber length between top 75 hubs by degree. **i**, Mean number of modules between hubs (Louvain community algorithm with $\gamma = 0.075$). **j**, Mean density of edges between hubs. Brain surrogates generated with G_r . Graphs in **c–j** generated with 10,000 randomizing trials.

combine to yield composite outcomes, such as the left–right asymmetries in fragility amongst the prefrontal hubs (Fig. 5f).

We quantified the fragility of hubs, defined as $1 - \phi$, where ϕ is the proportion of randomization required to cause P^h to fall below a value of 80% (Fig. 5b). Mapping the fragility of the original hubs (Fig. 5f) confirms that the most fragile hubs are located in heteromodal regions of prefrontal cortex and posterior areas that are

classically positioned at the apex of the brain's functional hierarchies³¹. To test this observation, we benchmarked our measure of hub fragility against a hierarchical decomposition of functional neuroimaging data. In particular, analyses of resting-state functional MRI data yield two hierarchical gradients: transmodal-to-unimodal regions ranked down the first gradient, while unimodal systems split into separate domains along a second gradient^{32,33}.

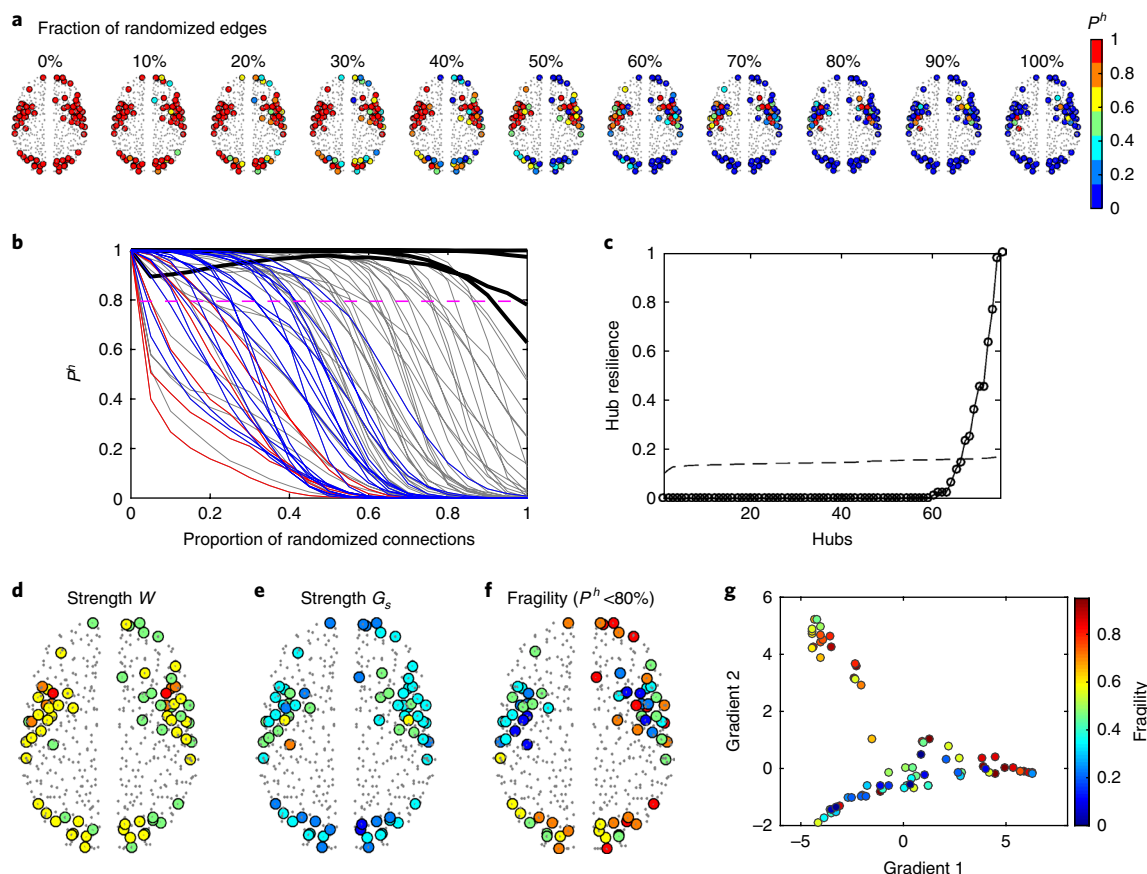


Fig. 5 | Fragility of hubs. **a**, Probability P^h that original hubs will remain hubs after randomizing a fraction of edges (G_s). **b**, Evolution of P^h for the 75 hubs (one line per hub). Bold curves represent the four hubs most likely to retain their hubness for the completely randomized brain surrogate. The fragility of the hubs is defined as $1 - \phi$, where ϕ is the proportion of randomization required to cause P^h to fall below 0.8. Red lines, frontal nodes (Montreal Neurological Institute (MNI) y-coordinate > 45); blue lines, posterior nodes (MNI y-coordinate < -60). **c**, Hub resilience minus the probability of original hubs to remain hubs when all edges have been randomized. Circles, G_s ; dashed line, R_s . **d**, Normalized strength of the original hubs before randomization. **e**, Normalized strengths of original hubs after randomizing all edges. **f**, Fragility of hubs. Colors as in **a**. **g**, Scatter plot of the first two connectivity-embedding gradients averaged over the nonzero voxels within regions. Regions are color-coded by their fragility index. Fragility increases with gradient 1 and gradient 2 (see also Supplementary Fig. 7 for correlation between fragility and the sum of gradients 1 and 2). Fig. generated with 5,000 randomizing trials.

We find a highly significant correlation between this measure of functional hierarchy (sum of gradients 1 and 2) and the structural fragility of hubs in our data ($r=0.43$, $P=0.00012$, 95% confidence interval (CI) [0.225, 0.600]; Fig. 5g and Supplementary Fig. 7).

Fragility and gray matter deterioration in schizophrenia. Hubs appear highly susceptible to the impact of brain pathology^{27,28}. In schizophrenia, regional gray matter volume loss³⁴ and cortical thinning³⁵ are most extensive in areas that contain a disproportionate number of structural hubs, such as temporal and prefrontal cortices³⁶. An elevated rate of gray matter decline is a key neurobiological feature of schizophrenia^{22,36}. We conjectured that the fragility of hub regions would predict the spatial distribution of accelerated cortical thinning in schizophrenia and that this effect would be stronger than the association of cortical thinning with hub strength.

To test this, we studied the association of our fragility index (Fig. 5f) with the rate of increased gray matter loss in patients with schizophrenia. Specifically, we tested whether regional variation in the rate of gray matter loss correlated with regional variation in hub fragility. Regional rates of gray matter loss were quantified with voxel-based morphometry (see Methods) in schizophrenia patients ($n=218$) and healthy controls ($n=167$). For each of 116 cortical and subcortical regions, a general linear model was fitted to quantify the influence on gray matter volume of diagnostic status, age,

square of age, and all two-way interactions between these factors. The rate of gray matter volume loss (mm^3/year), which varied as a function of age, was substantially faster in schizophrenia patients at ages 30–45 within the frontal, cingulate, temporal, occipital, and cerebellar cortices, as well as in the caudate nucleus and thalamus²².

Regional variation in hub fragility was correlated with regional variation in gray matter volume (i) in controls (Fig. 6a; 20–50 years, $P<0.05$, false discovery rate (FDR)-corrected) and (ii) in patients (Fig. 6b; 20–50 years), as well as (iii) the difference in the rate of gray matter decline between patients and controls (Fig. 6c; 20–38 years) and (iv) the relative difference ((patients – controls)/controls) in the rate of decline (Fig. 6d; 20–38 years). These results indicate that the most fragile regions coincide with the regions that show the fastest rates of gray matter atrophy in schizophrenia patients ($r=0.36$, $P=0.0014$, two-tailed, 95% CI [0.148, 0.545]; Fig. 6e). This is reflected in the accelerated deterioration of gray matter in schizophrenia, after normalizing for the effect in healthy controls (Fig. 6d). As with the subtle asymmetry in fragility, this effect is visually most notable in the right hemisphere. As a comparison, we also tested the association of gray matter deterioration with the strength of cortical hubs, a proxy to test the ‘hubopathy’ hypothesis^{27,37,38}. Hub strength was not significantly correlated ($P>0.05$, FDR-corrected) with gray matter deterioration and was thus a poorer predictor for gray matter deterioration than hub fragility in these data (Supplementary Fig. 8).

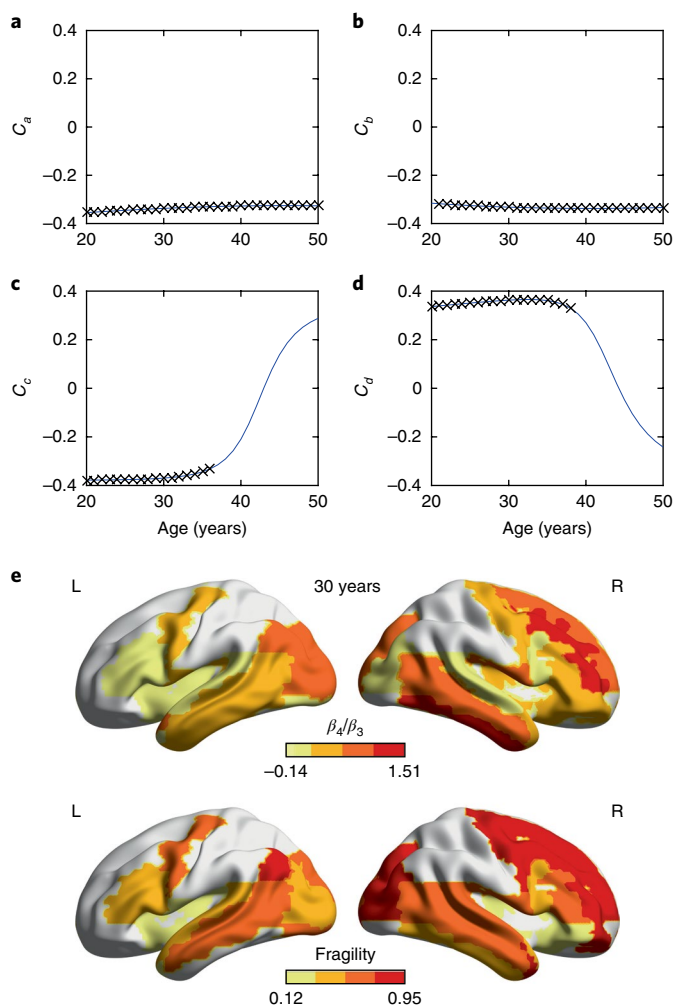


Fig. 6 | Fragility as a predictor for gray matter changes in schizophrenia.

a–d, Pearson correlation between fragility and the explanatory variable parameters of the quadratic generalized linear model as a function of age for each hub region ($n = 75$). **(a)** C_a indicates the correlation between fragility and the gray matter volume dependence on age for healthy controls (β_1 in equation (1) of Methods). **(b)** C_b indicates the correlation between fragility and the gray matter volume dependence on age for patients ($\beta_1 + \beta_2$). **(c)** C_c indicates the correlation between fragility and the difference in the rate of decay between patients and controls (patients – controls; β_4). **(d)** C_d indicates the correlation between fragility and the relative difference in the rate of decay between patients and controls ((patients – controls)/controls; β_4/β_3). Positive values of C_d indicate that fragile hubs have higher decay rates in patients than in controls. Black crosses indicate statistically significant correlations ($P < 0.05$, FDR-corrected). **e**, Spatial values of β_4/β_3 at age 30 and the average fragility of hub regions in the brain ($r = 0.36$, $P = 0.0014$). The corresponding values for the other correlations at age 30 are $C_a = -0.342$, $P = 0.0031$; $C_b = -0.33$, $P = 0.0036$; $C_c = -0.37$, $P = 0.0011$.

Phenotypic variability is a hallmark of schizophrenia, reflected in the severity, chronicity, and diversity of symptoms. We conjectured that interindividual phenotypic variability within the schizophrenia cohort would reflect the involvement of fragile hubs in the associated gray matter changes. In particular, we hypothesized that a greater overlap between gray matter loss and fragile hubs would be correlated with an earlier age-of-onset of schizophrenia, a stable trait marker of disease severity and poor outcome³⁹. We indeed observed a significant association ($r = -0.13$, $P = 0.028$, one-tailed,

95% CI $[-0.245, -0.019]$), between the involvement of fragile hubs in gray matter loss and earlier age of onset, an important indicator of likely future chronicity.

Discussion

The trade-off between parsimony and complexity is a fundamental evolutionary principle that shapes all biological systems. We studied this trade-off using randomizations of the human connectome, constrained to conserve wiring length and hence control parsimony while degrading complexity. By applying incremental perturbations, we were able to study the stochastic neighborhood of the human brain and hence quantify the fragility of network hubs. Our findings suggest that the connectome resides near a volatile topological regime, with a constellation of highly fragile hubs whose regional distribution overlaps with gray matter loss in schizophrenia. Moreover, there exists only a very small fraction of slightly perturbed networks that are ‘improved’, i.e., that show lower cost and higher complexity, small-world index, and modularity. This fraction reduces even further with deeper randomization.

Hubs are crucial for neuronal communication, are widely distributed, and form a richly connected backbone of the brain^{4,25}. Although hub-to-hub connections are longer than average⁷, our results show that in the presence of such highly connected hubs, the brain’s wiring cost is largely optimized for small permutations. That is, although some permutations can reduce wiring cost while retaining strong hub connectivity, their likelihood is small and limited to a minor fraction of randomized edges. Strong randomization yields surrogate networks with shorter total wiring cost, but with spatially peripheral hubs replaced by a highly connected central core and with a substantial loss of network complexity. If the actual spatial distribution of hubs is preserved, then the wiring cost of surrogate networks is almost always higher than that of the real brain. Assuming that the spatial distribution of hubs is required for local circuits to connect efficiently to the global workspace^{7,9}, our analyses suggest that the human brain is close to a configuration with minimal wiring cost. Hence the specific topological arrangement of the empirical connectome, including the position of its hubs, is ‘soft optimal’ (at an optimum point for the mean of cost and complexity metrics) and very nearly ‘hard optimal’ (even when considering the stochastic variability of the network perturbations).

Complexity is a rubric term that encompasses many aspects of natural systems. We employed a measure of functional complexity that rests on the behavior of weakly stable dynamics, predicted to arise when local elements interact through the network. We find that this measure decreases monotonically with progressive, geometrically preserving randomization. We also studied the modular (community) organization of the original and surrogate networks, which imbues a network with a balance between functional integration within communities and functional integration across modules⁵. The modularity of the surrogate networks decreases monotonically with randomization. In addition, high-strength hubs in the empirical connectome have a relatively low participation index, that is, they connect strongly within their local communities. As such, these peripherally located hubs are well positioned to influence the local modules in which they are embedded. The correlation is weakly positive in fully randomized networks. That is, the overall modularity is weaker in randomized networks and what remains is weakly determined by node strength.

Studying the nature of hub-to-hub connections under the influence of accumulating randomization reveals an intriguing topological transition. With progressive randomization, the brain exhibits multiple complex and distinct configurations, disconnecting hub-regions located at the extremities and strengthening regions in more central spatial positions. With relatively modest network perturbation, connectivity amongst the most fragile hubs differs markedly between different realizations, i.e., the stochastic ‘daughter’ networks

show high volatility. The presence of a highly volatile regime separating an ordered (original) from a disordered (randomized) state is characteristic of a phase transition in a complex system⁴⁰. This is consistent with the decrease in the functional complexity—which is at a maximum in a critical system perched between disordered and synchronous dynamics²⁴—and the increase in its variability, another hallmark of a phase transition. Notably, phase transitions in many complex systems exhibit peaks in different measures of volatility at slightly different points (Griffiths phase transitions⁴¹), as we observe here (for example, Fig. 4c,d,h). As noted above, a certain degree of variability is likely adaptive, because a species with insufficient diversity risks occupying a very narrow ecological niche¹². However, the diversity expressed with deeper randomization in our moderately perturbed networks may exceed this optimal set point, as the ensuing phenotypes diverge. Put alternatively, the proximity of the connectome to a region of topological volatility may act as a weak evolutionary influence, balancing the advantages of phenotypic variability against the consequences of unopposed random drift. As a result, those regions with a later evolutionary and brain maturational trajectory may be more fragile and hence susceptible to pathological perturbation.

Network perturbations may be considered as a first-order approximation of the combined effects of mutation, environmental influences, and genetic recombination on intergenerational changes in the connectome. The present work focusses on purely random and progressive (cost-preserving) perturbations, with no external influence and no adaptive selection. Nonetheless, we do find a finite, albeit very small, fraction of slightly perturbed connectomes that have a lower cost and a higher complexity. This shows that the connectome is not hard optimal, that is, there exists a small chance of finding more optimal configurations by chance. Future work could make the link to evolution more direct by employing genetic algorithms^{42,43} to iteratively generate new (perturbed but constrained) networks and simulate progressive generational changes under the influence of the cost functions considered here to yield generations of new connectomes with lower wiring cost and higher small-world index, complexity, and modularity. Although the present approach may provide insights into the cost–benefit factors impinging upon the human connectome, understanding the longitudinal trajectory that led to the present configuration would require additional insights from ecology and comparative connectomics⁹.

Heterogeneity is a hallmark of schizophrenia, reflected in its complex genetic architecture, neurobiological underpinnings, and phenotypic expression. These observations suggest that schizophrenia is not a unitary construct, but may be better conceptualized as a constellation of disorders, each representing a distinct excursion from adaptive neurocognitive function. Motivated by the notion that schizophrenia represents the outcome of a diverse array of white matter perturbations during different neurodevelopmental stages^{44,45}, we investigated a link between accelerated gray matter loss in schizophrenia²² and hub fragility. This extends the recent hubopathy hypothesis, in which hub regions that have larger metabolic costs are more vulnerable in schizophrenia^{27,46}, by ensuring that the resulting perturbations preserve wiring length. We found that the fragility index indeed more accurately predicts between-group differences in gray matter volume than hub strength. Hub regions consistently implicated in schizophrenia, such as medial frontal and superior temporal gyri³⁶, are particularly fragile. This effect is present in age-related effects within and between groups (Fig. 6a–c), as well as in the accelerated gray matter loss in schizophrenia until age 40 (Fig. 6d); it is possible that this accelerating difference reaches a plateau toward the end of the third decade and the normal aging effect begins to catch up. Note that our constrained perturbations do not specifically target hub regions by design: hub fragility and topological volatility rather emerge through the interaction of topological and geometric

factors. These observations thus support the notion that neurobiological changes in schizophrenia canvass a diverse range of brain network mutations under competing physical and biological constraints.

We focused on how geometry constrains brain network perturbations. Other factors also impact on the economy–complexity trade-off. Preservation of topological properties (such as modularity or clustering) yield alternative benchmark networks²⁴ that do not preserve wiring length but would permit a complementary perspective onto the present problem. The constraints imposed by fitting white matter bundles into the constrained intracranial volume—the packing problem—were addressed through the analysis of the corpus callosum. Additional packing constraints may prohibit networks with predominantly central hubs and a resulting core of high-volume, dense interconnectivity. Packing constraints may thus partly explain the peripheral location of hubs in empirical data. Moreover, understanding the geometry–topology relationship can also be inverted. That is, how do core topological properties, conserved across species⁹ (hubs, clustering, hierarchies, and a core–periphery structure), influence brain geometry? We have exclusively considered perturbations that rewire connections (i.e., constraining density). However, adding (development) or removing (degeneration) connections are alternative ways to study the trade-off between wiring cost and complexity.

The present work opens several lines of inquiry. The association of fragile hubs with gray matter volume decline in schizophrenia predicts a corresponding association with connectome changes in the illness that could be studied using tractography. Data from cross-sectional studies of cohorts at different stages of the illness do suggest a progression from circumscribed inter-hemispheric changes in anterior commissural connections in first-episode psychosis to such changes becoming widespread in those with chronic schizophrenia¹⁴. While these observations are consistent with our prediction, a more definitive test would require the analysis of longitudinal changes in those developing the disorder. This would also permit insights into hub fragility from a developmental perspective, addressing how schizophrenia may reflect diverse pathological processes by studying the transition into illness onset³⁹. Likewise, hub fragility could be applied to longitudinal studies of development, aging, and neurodegenerative illnesses, in which prefrontal hubs figure highly^{47,48}. Superimposing hierarchical theories of predictive coding⁴⁹ or models of large-scale cortical activity⁵⁰ could link these structural brain network disturbances to cognitive phenotypes.

Methods

Methods, including statements of data availability and any associated accession codes and references, are available at <https://doi.org/10.1038/s41593-018-0188-z>.

Received: 27 November 2017; Accepted: 30 May 2018;

Published online: 23 July 2018

References

1. Bullmore, E. & Sporns, O. The economy of brain network organization. *Nat. Rev. Neurosci.* **13**, 336–349 (2012).
2. Honey, C. J., Kötter, R., Breakspear, M. & Sporns, O. Network structure of cerebral cortex shapes functional connectivity on multiple time scales. *Proc. Natl Acad. Sci. USA* **104**, 10240–10245 (2007).
3. Bassett, D. S. et al. Hierarchical organization of human cortical networks in health and schizophrenia. *J. Neurosci.* **28**, 9239–9248 (2008).
4. van den Heuvel, M. P. & Sporns, O. Rich-club organization of the human connectome. *J. Neurosci.* **31**, 15775–15786 (2011).
5. Sporns, O. & Betzel, R. F. Modular brain networks. *Annu. Rev. Psychol.* **67**, 613–640 (2016).
6. Roberts, J. A. et al. The contribution of geometry to the human connectome. *Neuroimage* **124**, 379–393 (2016). Pt A.
7. van den Heuvel, M. P., Kahn, R. S., Goñi, J. & Sporns, O. High-cost, high-capacity backbone for global brain communication. *Proc. Natl Acad. Sci. USA* **109**, 11372–11377 (2012).

8. Rilling, J. K. Human and nonhuman primate brains: are they allometrically scaled versions of the same design? *Evol. Anthropol.* **15**, 65–77 (2006).
9. van den Heuvel, M. P., Bullmore, E. T. & Sporns, O. Comparative connectomics. *Trends Cogn. Sci.* **20**, 345–361 (2016).
10. Herculano-Houzel, S. The remarkable, yet not extraordinary, human brain as a scaled-up primate brain and its associated cost. *Proc. Natl Acad. Sci. USA* **109** Suppl 1, 10661–10668 (2012).
11. Frankel, N. W. et al. Adaptability of non-genetic diversity in bacterial chemotaxis. *eLife* **3**, e03526 (2014).
12. Schindler, D. E. et al. Population diversity and the portfolio effect in an exploited species. *Nature* **465**, 609–612 (2010).
13. Friston, K. Life as we know it. *J. R. Soc. Interface* **10**, 20130475 (2013).
14. Zalesky, A. et al. Disrupted axonal fiber connectivity in schizophrenia. *Biol. Psychiatry* **69**, 80–89 (2011).
15. Watts, D. J. & Strogatz, S. H. Collective dynamics of ‘small-world’ networks. *Nature* **393**, 440–442 (1998).
16. Fornito, A., Zalesky, A. & Breakspear, M. Graph analysis of the human connectome: promise, progress, and pitfalls. *Neuroimage* **80**, 426–444 (2013).
17. Sporns, O. & Zwi, J. D. The small world of the cerebral cortex. *Neuroinformatics* **2**, 145–162 (2004).
18. Harris, J. J. & Attwell, D. The energetics of CNS white matter. *J. Neurosci.* **32**, 356–371 (2012).
19. Horvát, S. et al. Spatial embedding and wiring cost constrain the functional layout of the cortical network of rodents and primates. *PLoS Biol.* **14**, e1002512 (2016).
20. Samu, D., Seth, A. K. & Nowotny, T. Influence of wiring cost on the large-scale architecture of human cortical connectivity. *PLOS Comput. Biol.* **10**, e1003557 (2014).
21. Henderson, J. A. & Robinson, P. A. Using geometry to uncover relationships between isotropy, homogeneity, and modularity in cortical connectivity. *Brain Connect.* **3**, 423–437 (2013).
22. Croypley, V. L. et al. Accelerated gray and white matter deterioration with age in schizophrenia. *Am. J. Psychiatry* **174**, 286–295 (2017).
23. Salvador, R. et al. Neurophysiological architecture of functional magnetic resonance images of human brain. *Cereb. Cortex* **15**, 1332–1342 (2005).
24. Zamora-López, G., Chen, Y., Deco, G., Krügelbach, M. L. & Zhou, C. Functional complexity emerging from anatomical constraints in the brain: the significance of network modularity and rich-clubs. *Sci. Rep.* **6**, 38424 (2016).
25. Mišić, B. et al. Cooperative and competitive spreading dynamics on the human connectome. *Neuron* **86**, 1518–1529 (2015).
26. Fulcher, B. D. & Fornito, A. A transcriptional signature of hub connectivity in the mouse connectome. *Proc. Natl Acad. Sci. USA* **113**, 1435–1440 (2016).
27. Crossley, N. A. et al. The hubs of the human connectome are generally implicated in the anatomy of brain disorders. *Brain* **137**, 2382–2395 (2014).
28. Fornito, A., Zalesky, A. & Breakspear, M. The connectomics of brain disorders. *Nat. Rev. Neurosci.* **16**, 159–172 (2015).
29. Colomer-de-Simón, P. & Boguñá, M. Double percolation phase transition in clustered complex networks. *Phys. Rev. X* **4**, 041020 (2014).
30. Gollo, L. L., Copelli, M. & Roberts, J. A. Diversity improves performance in excitable networks. *PeerJ* **4**, e1912 (2016).
31. Mesulam, M.-M. From sensation to cognition. *Brain* **121**, 1013–1052 (1998).
32. Margulies, D. S. et al. Situating the default-mode network along a principal gradient of macroscale cortical organization. *Proc. Natl Acad. Sci. USA* **113**, 12574–12579 (2016).
33. Huntenburg, J. M., Bazin, P.-L. & Margulies, D. S. Large-scale gradients in human cortical organization. *Trends Cogn. Sci.* **22**, 21–31 (2018).
34. Steen, R. G., Mull, C., McClure, R., Hamer, R. M. & Lieberman, J. A. Brain volume in first-episode schizophrenia. *Br. J. Psychiatry* **188**, 510–518 (2006).
35. Kuperberg, G. R. et al. Regionally localized thinning of the cerebral cortex in schizophrenia. *Arch. Gen. Psychiatry* **60**, 878–888 (2003).
36. Takahashi, T. et al. Progressive gray matter reduction of the superior temporal gyrus during transition to psychosis. *Arch. Gen. Psychiatry* **66**, 366–376 (2009).
37. Gollo, L. L., Zalesky, A., Hutchison, R. M., van den Heuvel, M. & Breakspear, M. Dwelling quietly in the rich club: brain network determinants of slow cortical fluctuations. *Phil. Trans. R. Soc. Lond. B* **370**, 20140165 (2015).
38. Rubinov, M. & Bullmore, E. Schizophrenia and abnormal brain network hubs. *Dialog. Clin. Neurosci.* **15**, 339–349 (2013).
39. Gogtay, N., Vyas, N. S., Testa, R., Wood, S. J. & Pantelis, C. Age of onset of schizophrenia: perspectives from structural neuroimaging studies. *Schizophr. Bull.* **37**, 504–513 (2011).
40. Cocchi, L., Gollo, L. L., Zalesky, A. & Breakspear, M. Criticality in the brain: a synthesis of neurobiology, models and cognition. *Prog. Neurobiol.* **158**, 132–152 (2017).
41. Moretti, P. & Muñoz, M. A. Griffiths phases and the stretching of criticality in brain networks. *Nat. Commun.* **4**, 2521 (2013).
42. Sporns, O., Tononi, G. & Edelman, G. M. Theoretical neuroanatomy: relating anatomical and functional connectivity in graphs and cortical connection matrices. *Cereb. Cortex* **10**, 127–141 (2000).
43. Goñi, J. et al. Exploring the morphospace of communication efficiency in complex networks. *PLoS One* **8**, e58070 (2013).
44. Friston, K. J. The disconnection hypothesis. *Schizophr. Res.* **30**, 115–125 (1998).
45. Pantelis, C. et al. Structural brain imaging evidence for multiple pathological processes at different stages of brain development in schizophrenia. *Schizophr. Bull.* **31**, 672–696 (2005).
46. Collin, G., Kahn, R. S., de Reus, M. A., Cahn, W. & van den Heuvel, M. P. Impaired rich club connectivity in unaffected siblings of schizophrenia patients. *Schizophr. Bull.* **40**, 438–448 (2014).
47. Douaud, G. et al. A common brain network links development, aging, and vulnerability to disease. *Proc. Natl Acad. Sci. USA* **111**, 17648–17653 (2014).
48. Perry, A. et al. The organisation of the elderly connectome. *Neuroimage* **114**, 414–426 (2015).
49. Stephan, K. E., Friston, K. J. & Frith, C. D. Dysconnection in schizophrenia: from abnormal synaptic plasticity to failures of self-monitoring. *Schizophr. Bull.* **35**, 509–527 (2009).
50. Breakspear, M. Dynamic models of large-scale brain activity. *Nat. Neurosci.* **20**, 340–352 (2017).

Acknowledgements

The authors thank the chief investigators and manager of the ASRB: V. Carr, U. Schall, R. Scott, A. Jablensky, B. Mowry, P. Michie, S. Catts, F. Henskens, and C. Loughland. The authors acknowledge the support of the National Health and Medical Research Council of Australia (APP1110975 to L.L.G.; APP1145168 and APP1144936 to J.R.; APP1037196, APP1118153, and APP1095227 to M.B.; APP1047648 to A.Z.; and ID1105825 to C.P.) and the Australian Research Council (CE140100007). The Australian Schizophrenia Research Bank (ASRB) is supported by the NHMRC (enabling grant 386500), the Pratt Foundation, Ramsay Health Care, the Viertel Charitable Foundation, and the Schizophrenia Research Institute.

Author contributions

L.L.G., J.A.R., A.Z., and M.B. designed the research and wrote the manuscript. L.L.G., J.A.R., and M.B. analyzed the data. L.L.G. prepared the figures. J.A.R. and A.Z. contributed new analytic tools. V.L.C., M.A.D.B., C.P., and A.Z. contributed the schizophrenia neuroimaging data. All authors contributed to editing and revising the manuscript.

Competing interests

The authors declare no competing interests.

Additional information

Supplementary information is available for this paper at <https://doi.org/10.1038/s41593-018-0188-z>.

Reprints and permissions information is available at www.nature.com/reprints.

Correspondence and requests for materials should be addressed to L.L.G. or M.B.

Publisher's note: Springer Nature remains neutral with regard to jurisdictional claims in published maps and institutional affiliations.

Methods

Diffusion MRI acquisition. We derived estimates of whole brain structural connectivity from diffusion images of 75 healthy subjects (aged 17–30 years; 47 females). Diffusion MRI data were acquired on a Philips 3 T Achieva Quasar Dual MRI scanner (Philips Medical Systems, Best, Netherlands) using a single-shot echoplanar imaging (EPI) sequence (TR = 7,767 ms, TE = 68 ms). To correct for head motion, the gradient direction matrix was rotated using a custom in-house algorithm. To reduce spatial intensity inhomogeneities, bias field correction was performed on the b0 image and subsequently applied to all diffusion-weighted (DW) images. Full details on data acquisition and preprocessing are as previously described⁶; see the Reporting Summary.

The gray matter was divided into 513 brain regions using an approximately equal-volume random subdivision of the automated anatomical labeling (AAL) parcellation^{51,52}. The resulting size of the ensuing parcels appropriately balances the accuracy of the streamlines (particularly their termination at the gray–white matter interface of the parcels) with the need to have sufficiently numerous nodes to undertake the incremental geometric perturbations required for the analyses⁶.

Tractography reconstruction. Corticocortical connectivity was reconstructed from diffusion MRI data using spherical deconvolution and densely seeded probabilistic tractography⁵³; see the Reporting Summary. Accordingly, tractograms were generated using a probabilistic streamline algorithm, which produces a set of connection trajectories by randomly sampling from the orientation uncertainty inherent in each FOD along the streamline paths. The weights for this connectome correspond to the number of streamlines connecting pairs of gray matter regions, normalized to the interareal distance (the curved fiber length). Similar to tract-tracing data in other human⁵⁴ and mammalian brains¹⁹, these weights span five orders of magnitude, exhibiting an exponential decay with distance⁵⁵. Because curved streamlines are always longer than the Euclidean distance, this does have a subtle, albeit systematic effect on the weight–length relationship (see Fig. 1 of ref. ⁶). The resulting connectome (averaged across subjects⁶) was a densely connected network. For calculation of graph metrics, we used 30% density (applied after any randomization), unless otherwise stated, eliminating edges with weights weaker than a threshold. As in our prior work^{6,48}, hubs were defined as the top 75 (15%) of nodes, ranked by strength. The principal findings are robust to modest changes in this number.

Partial randomization algorithms. To randomize connectomes, we randomly shuffle connection weights of the connectivity matrix using variants of two different schemes, either ignoring or preserving the brain geometry. Geometry-ignoring randomization (R) is the simplest and least-constrained surrogate network. This involves shuffling the weights indiscriminately, and so does not preserve the weight–distance relationship that is observed in the human connectome. Geometry-preserving randomization (G) involves randomizing under the constraint that the weight–distance relationship is (approximately) conserved⁶. We divide the set of connection weights into 100 equal-width bins by streamline length, and randomize only nodes contained within each bin. That is, we only shuffle weights between connections of similar length, thus preserving the weight–distance relationship. The use of 100 bins ensures a sufficiently fine-grained decomposition of the length–weight relationship, hence preserving its complex nature (and preserving the null). The use of too many bins leads to too few edges within each bin and impoverishes the number of distinct surrogate realizations (i.e., the ensemble of nulls will not span the full null distribution). Between these extremes, the algorithm is very robust to modest changes in the number of bins.

Both randomizations (ignoring and preserving geometry) is performed on the unthresholded connectome and followed by the thresholding procedure to yield R_w and G_w , respectively. Because our original group-average network is densely connected, we are able to shuffle without the complications of edge-rewiring algorithms⁵⁶, though our methods also generalize to that setting. Although the weight distribution is preserved (weights are simply shuffled), the mixing of rows and columns renders the node-strength distribution of R_w and G_w more Gaussian than the empirical distribution. A node-strength correction step is thus applied to both randomizations to restore the original node-strength distribution⁶. The correction algorithm involves iteratively updating the in-degree and out-degree of nodes (sums of the rows and columns). First the weights are multiplied by the ratio of the node's original strength and its current strength. Next, the network is made symmetric by averaging it with its transpose. This procedure is then repeated until the distributions of node strength converge to the empirical one. This procedure can optionally preserve the strength distribution (R and G) or, by reordering the node numbering to match the original rank-order, preserve the original sequence of strength distribution (R_w and G_w). To partially randomize a subset of the connectivity matrix, only a randomly selected subset of weights is shuffled.

Graph-theory measures. Node strength is the sum of the connection weights. Small-worldness is computed as C/L^{57} , where C is the clustering coefficient of the binary network divided by the clustering coefficient of the completely randomized binary connectome R_w , and L is the path length of the binary network divided

by the path length of R_w . Binary networks are calculated by setting all nonzero elements to unity after thresholding the weighted networks. C and L (and hence the small-world index) are the only graph metrics in the study derived using binary networks.

Modularity is computed in the weighted subnetwork composed of hubs and their interhub connections using the Louvain algorithm with $\gamma = 0.075^{58,59}$. This parameter controls the size of the modules. Comparable results are obtained across a range of similar values of γ . Clustering, path length, and modularity are computed using the Brain Connectivity Toolbox⁵⁹.

To compute network susceptibility, χ , the s.d. of node strength across trials is evaluated for each node. This quantity is then averaged across all nodes.

Hub fragility. For any hub in the original connectome, let P^h be the probability that it is a hub in a G_r surrogate network after a fraction of network randomization (where the probability is taken over an ensemble of realizations). Then define ϕ as the fraction of randomized connections required to reduce P^h to a value less than 0.8 (Fig. 5b). The fragility of that hub is defined as $1 - \phi$. Hence, if ϕ is very small (i.e., the strength of a hub decays very quickly for a small fraction of randomization), then that hub will possess high fragility.

Complexity. We used an analytical measure of complexity that has been recently proposed by Zamora-Lopez and colleagues²⁴. This complexity measure estimates the normed entropy of a distribution of functional connections (linear correlations), and it increases as the distribution of linear correlations approaches a uniform distribution on the interval $[-1, 1]$: linear correlations that are all high or near zero have a highly nonuniform distribution and thus take the minimum value of zero. In a proposed analytical solution²⁴, the functional connectivity obtained from a structural connectome is generated by a simple Gaussian diffusion model and is a function of a parameter that couples individual nodes through the corresponding network. The final measure, which we term 'functional complexity', corresponds to the peak of the ensuing entropy values (canvassed across a wide range of coupling strengths). We first normalized the weighted connectivity matrices by their largest eigenvalue, λ_{\max} , and scanned the coupling strength in the range 0–10, as the complexity peak falls within this range²⁴.

Cortical hierarchy. To estimate the hierarchical level of cortical regions, we used the principal gradient decomposition of connectivity data published by Margulies and colleagues³², available at <https://neurovault.org/collections/1598/>. To compare the gradient index in voxel space, we computed the average gradient value over all nonzero voxels within each hub region. The average gradient value was computed for the first two most relevant gradients³². The sum of the first two gradients, which recapitulates classic hierarchical arrangements of cortex³¹, was regressed against the fragility index.

Schizophrenia morphometry modeling. Gray matter volume was estimated in a sample of schizophrenia patients ($n = 218$) and age-matched healthy controls ($n = 167$). Sample demographics are shown in Supplementary Table 1. Details related to recruitment procedures have been reported elsewhere²². An optimized, magnetization-prepared rapid-acquisition gradient echo (MP-RAGE) image of brain anatomy was acquired in each individual using a Siemens Avanto 1.5-Tesla system (Siemens, Erlangen, Germany). The following acquisition parameters were used: 176 sagittal slices of 1-mm thickness without gap; field of view: 250×250 mm²; repetition time/echo time: 1,980/4.3 ms; data matrix size: 256×256 ; voxel dimensions: $0.98 \times 0.98 \times 1.0$ mm³. Maps of gray matter volume were calculated for each individual with optimized voxel-based morphometry (VBM8)⁶⁰, as implemented in statistical parametric mapping (SPM8) software. In brief, MP-RAGE images were segmented into gray matter, white matter, and cerebrospinal fluid. Gray matter segments were then spatially aligned to a high-dimensional diffeomorphic anatomical registration through exponentiated lie algebra (DARTEL) template ($1.5 \times 1.5 \times 1.5$ -mm isotropic voxels) in the MNI space that is provided with the VBM8 toolbox. Gray matter voxels were multiplied by the nonlinear components of this deformation (modulated normalized – nonlinear only) to provide a measure of the absolute amount of gray matter volume corrected for individual brain sizes. For each individual, a regionally averaged measure of gray matter volume was then computed for each of the 116 regions comprising the AAL atlas⁵². This was achieved by averaging the gray matter volume estimates for each voxel across all voxels comprising a region.

Statistics. For each region, the relation between gray matter volume, V , and age was modeled with the following general linear model,

$$V(i) = \beta_1 + \beta_2 \times \text{diagnosis}(i) + \beta_3 \times (\text{age}(i) - A) + \beta_4 \times (\text{age}(i) - A) \times \text{diagnosis}(i) + \beta_5 \times (\text{age}(i) - A)^2 + \beta_6 \times (\text{age}(i) - A)^2 \times \text{diagnosis}(i) + \epsilon(i) \quad (1)$$

where the diagnostic status and age of the i th individual are denoted with $\text{diagnosis}(i)$ and $\text{age}(i)$, respectively, and $\epsilon(i)$ is a normally distributed error

term²². We assume $diagnosis(i) = 1$ if the i th individual is a patient, otherwise $diagnosis(i) = 0$. This yielded explanatory variables $\beta_1, \beta_2, \dots, \beta_6$:

- β_1 is the intercept (constant) term (the gray matter volume in controls),
- β_2 is the between-group difference in gray matter volume at age A ,
- β_3 is the rate of gray matter loss in controls at age A ,
- β_4 is the between-group difference in gray matter loss at age A ,
- β_5 is the change in rate of gray matter loss in controls, and
- β_6 is the between-group difference in change in rate of gray matter loss.

The regression model defined by the equation above was independently fitted, with age centered between 20 and 50 years in yearly increments; that is, $A = 20, 21, \dots, 50$. Three participants (healthy controls; two females and one male) of age < 19 were not used in these analyses. When the regression was estimated with age centered at A , the amount of gray matter volume loss (β_1 and β_2) and the rate of gray matter volume loss (β_3 and β_4) specifically pertained to an age of A years. Therefore, fitting the model independently at each year yielded a cross-sectional map of gray matter volume across the adult lifespan in patients and controls²².

To test whether regional variation in hub fragility was associated with regional variation in gray matter volume loss, the Pearson correlation coefficient (degrees of freedom: 114) was computed between hub fragility and: (i) gray matter volume in controls (β_1); (ii) gray matter volume in patients ($\beta_1 + \beta_2$); (iii) difference in the rate of gray matter decline between patients and controls (β_3); (iv) relative difference ((patients – controls)/controls) in the rate of decline (β_4/β_3). Note that $\beta_1, \beta_2, \beta_3$, and β_4 are functionally dependent on age, A , and thus these correlations were independently assessed between 20 and 50 years in yearly increments. Family-wise error control for repeated tests across age was performed using the false discovery rate (FDR)⁶¹. For comparison with these previously published gray matter volume data, we preserve the assignment of gray matter volume to these larger AAL parcels. The fragility of each hub was correlated with the explanatory variable of the AAL parcel whose centroid was nearest to the centroid of the hub region at the finer parcellation. Note that, due to the heterogeneous size of the various AAL parcels, individual nodes with high fragility can be represented as relatively large surfaces (for example, middle temporal gyrus). Residuals of this correlation were found to be normally distributed by a Kolmogorov–Smirnov test ($P = 0.89$), justifying the use of a parametric correlation test.

Correlation with age of onset. For each of the 75 hub regions, we first determined the differences between the gray matter volume quadratic regression curve for schizophrenia patients ($V(i)$) and the volume of this brain region for each patient. The residuals of this regression for all hubs captures the within group variability (not captured by the group-wise model). We calculated the Pearson correlation of these residuals against the fragility index for each subject, yielding a subject-specific index of overlap (between fragility and gray matter loss). We then tested for a linear association between this index and the age of onset. Note that for this regression we used the $n = 206$ cases for whom full phenotypic data was available.

Sample size. This is predominantly a computational modeling study, using data to test model predictions from two independent datasets. These were existing and previously published datasets^{6,22}; see the Reporting Summary. Data collection

and analysis were not performed blind to the conditions of the experiments. Randomization of group assignment is not applicable to this study.

Ethics and consent. All data were analyzed following approval from the QIMR Berghofer Human Research Ethics Committee (HRECp1476). Written informed consent was obtained from all participants following local institutional ethics approval. The data used for the schizophrenia analyses were obtained from the Australian Schizophrenia Research Bank. Study procedures were approved by the Melbourne Health Human Research Ethics Committee. Written informed consent was obtained from all participants, following local institutional ethics approval. The authors have complied with all local institutional and national ethical regulations.

Reporting Summary. Further information on experimental design is available in the Nature Research Reporting Summary linked to this article.

Data availability. The data that support the findings of this study are available from the corresponding author upon reasonable request.

Code availability. The Matlab code to perform the partial randomization is provided as a Supplementary Software file and is available at <http://www.sng.org.au/Downloads>.

References

- Zalesky, A. et al. Whole-brain anatomical networks: does the choice of nodes matter? *Neuroimage* **50**, 970–983 (2010).
- Tzourio-Mazoyer, N. et al. Automated anatomical labeling of activations in SPM using a macroscopic anatomical parcellation of the MNI MRI single-subject brain. *Neuroimage* **15**, 273–289 (2002).
- Tournier, J., Calamante, F. & Connelly, A. MRtrix: diffusion tractography in crossing fiber regions. *Int. J. Imaging Syst. Technol.* **22**, 53–66 (2012).
- Hagmann, P. et al. Mapping the structural core of human cerebral cortex. *PLoS Biol.* **6**, e159 (2008).
- Roberts, J. A., Perry, A., Roberts, G., Mitchell, P. B. & Breakspear, M. Consistency-based thresholding of the human connectome. *Neuroimage* **145**, 118–129 (2017). Pt A.
- Alstott, J., Klymko, C., Pyzza, P. B. & Radcliffe, M. Local rewiring algorithms to increase clustering and grow a small world. Preprint at *arXiv* <https://arxiv.org/abs/1608.02883> (2016).
- Humphries, M. D. & Gurney, K. Network ‘small-world-ness’: a quantitative method for determining canonical network equivalence. *PLoS One* **3**, e0002051 (2008).
- Blondel, V. D., Guillaume, J.-L., Lambiotte, R. & Lefebvre, E. Fast unfolding of communities in large networks. *J. Stat. Mech.* **2008**, P10008 (2008).
- Rubinov, M. & Sporns, O. Complex network measures of brain connectivity: uses and interpretations. *Neuroimage* **52**, 1059–1069 (2010).
- Ashburner, J. & Friston, K. J. Voxel-based morphometry—the methods. *Neuroimage* **11**, 805–821 (2000).
- Benjamini, Y. & Hochberg, Y. Controlling the false discovery rate: a practical and powerful approach to multiple testing. *J. R. Stat. Soc. B* **57**, 289–300 (1995).

Reporting Summary

Nature Research wishes to improve the reproducibility of the work that we publish. This form provides structure for consistency and transparency in reporting. For further information on Nature Research policies, see [Authors & Referees](#) and the [Editorial Policy Checklist](#).

Statistical parameters

When statistical analyses are reported, confirm that the following items are present in the relevant location (e.g. figure legend, table legend, main text, or Methods section).

n/a Confirmed

- ☐ ☒ The exact sample size (n) for each experimental group/condition, given as a discrete number and unit of measurement
- ☐ ☒ An indication of whether measurements were taken from distinct samples or whether the same sample was measured repeatedly
- ☐ ☒ The statistical test(s) used AND whether they are one- or two-sided
Only common tests should be described solely by name; describe more complex techniques in the Methods section.
- ☐ ☒ A description of all covariates tested
- ☐ ☒ A description of any assumptions or corrections, such as tests of normality and adjustment for multiple comparisons
- ☐ ☒ A full description of the statistics including central tendency (e.g. means) or other basic estimates (e.g. regression coefficient) AND variation (e.g. standard deviation) or associated estimates of uncertainty (e.g. confidence intervals)
- ☐ ☒ For null hypothesis testing, the test statistic (e.g. F , t , r) with confidence intervals, effect sizes, degrees of freedom and P value noted
Give P values as exact values whenever suitable.
- ☒ ☐ For Bayesian analysis, information on the choice of priors and Markov chain Monte Carlo settings
- ☐ ☒ For hierarchical and complex designs, identification of the appropriate level for tests and full reporting of outcomes
- ☐ ☒ Estimates of effect sizes (e.g. Cohen's d , Pearson's r), indicating how they were calculated
- ☐ ☒ Clearly defined error bars
State explicitly what error bars represent (e.g. SD, SE, CI)

Our web collection on [statistics for biologists](#) may be useful.

Software and code

Policy information about [availability of computer code](#)

Data collection

Preprocessing of all diffusion-weighted (DW) images was performed using FSL (Smith et al. 2004).

All tractography data were then analysed using the freely available MRtrix software (Tournier et al., 2012).

All structural morphometric analyses were performed using VBM8 as implemented in SPM8 (<http://www.fil.ion.ucl.ac.uk/spm/software/spm8/>) running in Matlab R2014b <http://www.mathworks.com.au/products/matlab/>).

Data analysis

Matlab R2014b.

Our code for matrix randomization is available in the public domain (www.sng.org.au/Downloads).

For manuscripts utilizing custom algorithms or software that are central to the research but not yet described in published literature, software must be made available to editors/reviewers upon request. We strongly encourage code deposition in a community repository (e.g. GitHub). See the Nature Research [guidelines for submitting code & software](#) for further information.

Data

Policy information about [availability of data](#)

All manuscripts must include a [data availability statement](#). This statement should provide the following information, where applicable:

- Accession codes, unique identifiers, or web links for publicly available datasets
- A list of figures that have associated raw data
- A description of any restrictions on data availability

The structural connectivity data are available from the authors upon request.

Field-specific reporting

Please select the best fit for your research. If you are not sure, read the appropriate sections before making your selection.

☒ Life sciences ☐ Behavioural & social sciences ☐ Ecological, evolutionary & environmental sciences

For a reference copy of the document with all sections, see [nature.com/authors/policies/ReportingSummary-flat.pdf](https://www.nature.com/authors/policies/ReportingSummary-flat.pdf)

Life sciences study design

All studies must disclose on these points even when the disclosure is negative.

Sample size	This is predominantly a computational modelling study, using data to test model predictions from two independent data sets - a normative cohort of 75 healthy young adults (aged 17-30) for the structural connectome; and a large case-control study of 218 adults with schizophrenia and 167 age-matched controls (all aged 18-65) for the cortical morphometry. These were existing and previously published data sets. These sample sizes are sufficient to detect modest effect sizes as per Roberts et al. (2016) and Cropley et al. (2016) that previously used these datasets. Due to the discovery nature of the present modelling study, no explicit prior power calculations were possible.
Data exclusions	No data from these previously published studies were excluded from the present study.
Replication	We replicated our principal findings regarding economic wiring length across a broad range of connection densities (an important threshold) - please see Supplementary Figures 4 and 5. To ensure that our findings can be reliably reproduced, our code for matrix randomization (Figure 1 and Supplementary Figure 1) is available in the public domain (www.sng.org.au/Downloads) and as Supplementary Software. The structural connectivity data will be available upon request.
Randomization	This is not a randomized treatment study. Clinical participants were recruited from referring outpatient clinics. Controls were recruited by advertisement. All participants meeting specified exclusion and inclusion criteria were recruited into the study.
Blinding	Blinding is not relevant to this study because it is not a randomized treatment study.

Reporting for specific materials, systems and methods

Materials & experimental systems

n/a	Involved in the study
<input checked="" type="checkbox"/>	<input type="checkbox"/> Unique biological materials
<input checked="" type="checkbox"/>	<input type="checkbox"/> Antibodies
<input checked="" type="checkbox"/>	<input type="checkbox"/> Eukaryotic cell lines
<input checked="" type="checkbox"/>	<input type="checkbox"/> Palaeontology
<input checked="" type="checkbox"/>	<input type="checkbox"/> Animals and other organisms
<input type="checkbox"/>	<input checked="" type="checkbox"/> Human research participants

Methods

n/a	Involved in the study
<input checked="" type="checkbox"/>	<input type="checkbox"/> ChIP-seq
<input checked="" type="checkbox"/>	<input type="checkbox"/> Flow cytometry
<input type="checkbox"/>	<input checked="" type="checkbox"/> MRI-based neuroimaging

Human research participants

Policy information about [studies involving human research participants](#)

Population characteristics	We studied data to test model predictions from two independent data sets - a normative cohort of 75 healthy young adults (aged 17-30, 47 females) for the structural connectome; and a large case-control study of 218 adults with schizophrenia (62 females) and 167 age-matched controls (86 females) all aged 18-65. These were existing and previously published data sets.
----------------------------	---

Data for our clinical (schizophrenia) cohort was obtained from the Australian Schizophrenia Research Bank (ASRB). Exclusion criteria included any organic brain disorder, history of brain trauma followed by a long period of amnesia (> 24h), mental retardation (full-scale IQ < 70), movement disorders, current drug or alcohol dependence, as well as electroconvulsive therapy in the past 6 months. Healthy controls with a personal or family history of psychosis or bipolar I disorder were also excluded. Patients had a confirmed diagnosis of schizophrenia or schizoaffective disorder according to DSM-IV or ICD-10 diagnostic criteria.

Recruitment

Clinical participants were recruited from referring outpatient clinics. Controls were recruited by advertisement. All participants meeting specified exclusion and inclusion criteria were recruited into the study.

Magnetic resonance imaging

Experimental design

Design type

Computational modelling of cross sectional data from two independent cohorts. Structural connectivity data from 75 healthy young adults (age 17-30). Structural morphometric data from a case-control study of 218 adults with schizophrenia and 167 age-matched controls (all aged 18-65).

Design specifications

This is not a study of task-related or resting state fMRI.

All diffusion and structural MRI data were acquired according to standard protocols and as described in the Methods section.

Behavioral performance measures

There are no behavioural tasks in this study.

Acquisition

Imaging type(s)

Diffusion MRI and Structural MRI.

Field strength

dmRI were acquired at 3T and structural MRI data were acquired at 1.5T from 2 independent cohorts.

Sequence & imaging parameters

Diffusion MRI data were acquired for the first data set using a Philips 3 T Achieva Quasar Dual MRI scanner (Philips Medical System, Best, The Netherlands) using a single-shot echo-planar imaging (EPI) sequence (TR = 7767 ms, TE = 68 ms). Structural (T1-weighted) magnetic resonance imaging scans (sMRI) were acquired for the second data set with a Siemens Avanto 1.5-Tesla system (Siemens, Erlangen, Germany) across five different sites in Australia. Exactly the same acquisition sequence for T1-weighted scans was used across all sites. For T1-weighted images, an optimized magnetization-prepared rapid acquisition gradient echo (MP-RAGE) sequence was acquired with the following parameters: 176 sagittal slices of 1mm thickness without gap; field of view = 250 x 250 mm²; repetition time/echo time = 1980/4.3 ms; data matrix size = 256 x 256; voxel dimensions = 0.98 x 0.98 x 1.0 mm³.

Area of acquisition

Whole brain.

Diffusion MRI



Used



Not used

Parameters

For each diffusion scan, 32 gradient directions ($b = 1000$ s/mm²) and a non-diffusion-weighted acquisition ($b = 0$ s/mm²) were acquired over a 96×96 image matrix (field of view 240 mm x 240 mm x 137.5 mm), with a slice thickness of 2.5 mm and no gap, reconstructed to yield 1 mm x 1 mm x 2.5 mm voxels (where the longer dimension is along the dorsoventral axis). Two sets of diffusion scans were acquired for each subject.

Preprocessing

Preprocessing software

Preprocessing of all diffusion-weighted (DW) images was performed using FSL (Smith et al. 2004).

All tractography data were then analysed using the freely available MRtrix software (Tournier et al., 2012).

All structural morphometric analyses were performed using VBM8 as implemented in SPM8 (<http://www.fil.ion.ucl.ac.uk/spm/software/spm8/>) running in Matlab R2014b (<http://www.mathworks.com.au/products/matlab/>).

Normalization

Fractional anisotropy (FA) images were derived from subject-specific diffusion MRI data. The MNI T1 2 mm template was then co-registered to the subject's fractional anisotropy (FA) image. The parcellation template was transformed into subject space by applying the transformation matrix generated from registering the MNI template to the FA image.

Structural MRI data were aligned using a high-dimensional Diffeomorphic Anatomical Registration Through Exponentiated Lie Algebra (DARTEL) template (1.5x1.5x1.5mm isotropic voxels) in the MNI space that is provided with the VBM8 toolbox.

Normalization template

To derive structural connectivity matrices from the diffusion MRI data, anatomical nodes were pre-defined by subdividing the standard AAL (Tzourio-Mazoyer et al., 2002) template into 513 cortical and sub-cortical regions of approximately uniform size (Zalesky et al., 2010). Parcellations within single-subject space were achieved by employing affine linear registrations within the FSL software package (Smith et al., 2004).

As stated above, structural MRI were aligned in the MNI space provided with the VBM8 toolbox.

Noise and artifact removal

To correct for head motion, the gradient direction matrix was rotated using a custom algorithm available in MRtrix software (Tournier et al., 2012; Leemans and Jones, 2009; Raffelt et al., 2012). To reduce spatial intensity inhomogeneities, intensity normalisation was performed on the b0 image and subsequently applied to all diffusion-weighted (DW) images (Sled et al., 1998). Lastly, a Higher Order Model Outlier Rejection model (Pannek et al., 2012) identified voxels with residual outliers in the DWsignal.

Volume censoring

Volume censoring (or scrubbing) is a procedure reserved for the pre-processing of fMRI data which were not included in the present study.

Statistical modeling & inference

Model type and settings

(1) For the schizophrenia group analyses we computed a general linear model in which for each region i the relation between gray matter volume, $V(i)$, and age was modeled by:

$$V(i) = \beta_1 + \beta_2 \times \text{diagnosis}(i) + \beta_3 \times (\text{age}(i) - A) + \beta_4 \times (\text{age}(i) - A) \times \text{diagnosis}(i) + \beta_5 \times (\text{age}(i) - A)^2 + \beta_6 \times (\text{age}(i) - A)^2 \times \text{diagnosis}(i),$$

where the diagnostic status and age of the i -th individual are denoted with $\text{diagnosis}(i)$ and $\text{age}(i)$, respectively [43]. We assume $\text{diagnosis}(i) = 1$ if the i th individual is a patient, otherwise $\text{diagnosis}(i) = 0$. This yielded explanatory variables β_1 , β_2 , ..., β_6 :

β_1 is the intercept (constant) term (the grey matter volume in controls),
 β_2 is the between-group difference in gray-matter volume at age A ,
 β_3 is the rate of gray matter loss in controls at age A ,
 β_4 is the between-group difference in gray-matter loss at age A ,
 β_5 is the change in rate of gray matter loss in controls at age A , and
 β_6 is the between-group difference in change in rate of gray matter loss at age A .

(2) We also performed a linear regression of the parameters of the model with the fragility index obtained from our connectome analyses (Fig 6).

(3) Finally, we performed a linear regression at the individual level of the residuals of the above quadratic regression with the fragility index (Fig 6E).

Effect(s) tested

For the tests specified above:

- (1): The effect is gray matter loss as a function of age as per the above general linear model.
- (2): The effect is the correlation between fragility and the rate of gray matter loss.
- (3): The effect is the correlation of the residuals with the fragility index for each patient.

Specify type of analysis: ☐ Whole brain ☐ ROI-based ☒ Both

All analyses were performed at the whole brain level. There were no a priori region of interest analyses.

Anatomical location(s)

We did use an atlas-based parcellation as described above for the purposes of connectivity analyses. However we included all parcels from all gray matter regions in our analyses.

Statistic type for inference
(See [Eklund et al. 2016](#))

We did not analyse fMRI data and therefore did not perform voxel- or cluster-wise family-wise correction (as addressed in Eklund). We performed a general linear model as described above (1), in addition to correlations between novel graph metrics and gray matter changes in schizophrenia.

Correction

To correct for the multiple comparisons at different ages in test (2) above, we used the Benjamini & Hochberg (1995) method to obtain false discovery rate (FDR) corrected p-values at the 0.05 significance level.

Models & analysis

- n/a | Involved in the study
- ☒ ☐ Functional and/or effective connectivity
 - ☐ ☒ Graph analysis
 - ☐ ☒ Multivariate modeling or predictive analysis

Graph analysis

We used group-level structural connectivity data. Our independent variable was the fraction of randomized connections, and we compared various randomization methods.

We computed clustering coefficient, path length and small-world coefficient using binary connectomes with various densities.

We used weighted connectomes for all other graph theory-measures: wiring cost, fiber length, modularity, complexity, susceptibility and fragility.

The independent variables were age and diagnosis.

We did not perform machine learning classification, and there is no feature extraction or dimension reduction.

Multivariate modeling and predictive analysis